Filament extrusion-based additive manufacturing of 316L stainless steel: Effects of sintering conditions on the microstructure and mechanical properties

Author(s):
Wagner, Marius A.; Engel, Jona; Hadian, Amir; Clemens, Frank; Rodriguez-Arbaizar, Mikel; Carreño-Morelli, Efrain; Wheeler, Jeffrey M.; Spolenak, Ralph

Publication date:
2022-11

Permanent link:
https://doi.org/https://doi.org/10.3929/ethz-b-000574116

Originally published in:
Additive Manufacturing 59, https://doi.org/10.1016/j.addma.2022.103147

Additive Manufacturing 59 (2022) 103147

Contents lists available at ScienceDirect

Additive Manufacturing

journal homepage: www.elsevier.com/locate/addma

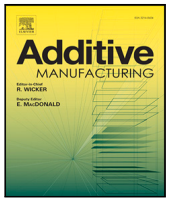

Research paper

Filament extrusion-based additive manufacturing of 316L stainless steel: Effects of sintering conditions on the microstructure and mechanical properties

Marius A. Wagner [a,*], Jona Engel [a], Amir Hadian [b], Frank Clemens [b], Mikel Rodriguez-Arbaizar [c], Efrain Carreño-Morelli [c], Jeffrey M. Wheeler [a], Ralph Spolenak [a,*]

[a] Laboratory for Nanometallurgy, Department of Materials, ETH Zürich, 8093 Zürich, Switzerland
[b] Laboratory for High Performance Ceramics, Empa, 8600 Dübendorf, Switzerland
[c] University of Applied Sciences and Arts Western Switzerland, 1950 Sion, Switzerland

ARTICLE INFO

Keywords:
Fused filament fabrication of metals
High-speed nanoindentation mapping
Sintering of 316L steel
Porosity analysis
Fused deposition modeling of metals

ABSTRACT

Filament extrusion-based additive manufacturing of metals offers an alternative to the widespread beam-based counterparts. The microstructure obtained from extrusion-based techniques differs greatly from the ones obtained by beam-based additive manufacturing, as a sintering process is used, in contrast to the rapid solidification of a melt pool. In this study, the microstructure of 316L stainless steel fabricated by filament extrusion is investigated as a function of debinding and sintering conditions. High-speed nanoindentation correlated with energy-dispersive X-ray mapping is employed for microstructural characterization.

High sintering temperatures of 1350 °C, an atmosphere of pure H_2, and a cooling rate of 60 K/m are found to result in the optimal microstructure. High densities are obtained due to accelerated densification, enabled by the introduction of diffusion paths due to δ-ferrite formation. At the same time, hard phases like oxides or σ-precipitates with detrimental effects on the mechanical properties can be avoided. It is shown that the porosity can be quantified by analysis of hardness and modulus data from nanoindentation mapping. The values obtained are in good agreement with optical and Archimedes immersion method measurements. Tensile tests of 3D-printed and sintered specimens show excellent ductility and strength in comparison to literature. We demonstrate that 3D printing of 316L filaments and sintering with the optimized conditions results in material properties comparable to bulk values.

1. Introduction

As one of the most used construction materials, the production of steel is an important component of the world's energy consumption and CO_2 emissions [1]. The transformation of the steel industry towards CO_2 neutrality imposes an extreme challenge [2]. In addition to reducing the emissions of steel production process, this problem can also be tackled by more efficient usage of the material. Additive fabrication technologies offer a promising approach for reduction of material waste compared to subtractive manufacturing techniques. Furthermore, additive manufacturing (AM) offers enormous geometrical design freedom and flexibility. Despite these assets, AM techniques often struggle to compete with non-additive techniques. One major challenge is obtaining mechanical properties similar to those of conventionally fabricated materials. Process-induced porosity, delamination due to residual stresses, or brittle secondary phases can adversely affect the mechanical properties of material fabricated by AM [3–5]. Extrusion-based AM of metals is a rapidly evolving technique, which stands out due to its low cost, anisotropy, and low health hazard [6,7].

Fused filament fabrication of metals (FFFm), like any other extrusion-based technique, relies on sintering to transform the raw material from a powder into a dense metal. All extrusion-based AM approaches require that a metal or ceramic powder is mixed with a polymeric binder to allow shaping, analogous to the widespread powder injection molding. After deposition, the binder is removed in a debinding step, and the remaining material is sintered. This sintering process plays an essential role in affecting the microstructure and hence the material properties. For good mechanical properties, the sintered material should have a high density and be free of defects and detrimental phases [8].

* Corresponding authors.
E-mail addresses: marius.wagner@mat.ethz.ch (M.A. Wagner), ralph.spolenak@mat.ethz.ch (R. Spolenak).

https://doi.org/10.1016/j.addma.2022.103147
Received 24 April 2022; Received in revised form 15 August 2022; Accepted 9 September 2022
Available online 13 September 2022

316L austenitic stainless steel is widely used due to its good corrosion resistance, high temperature strength [9] and weldability [10]. For this reason, 316L is one of the most researched materials in the field of FFFm. Numerous studies on filament-based fabrication of steel have investigated the print-porosity and its influence on the mechanical anisotropy [4,11–15], surface roughness [16,17], or fatigue [18]. The sintering process has fundamental effect on the final microstructure and the mechanical properties. the final microstructure after sintering was characterized [19] and the effect of the sintering temperature and time on the porosity has been studied [20]. Similar investigations have been performed for other metals like Mg alloys [21], Ti and its alloys [22–26], or Cu [27,28].

The final microstructures and consequently the obtained properties are greatly defined during the sintering step. This work focuses on the investigation of different sintering conditions for 316L stainless steel and their effect on the phases in the final material. One emerging tool for simultaneously investigation of both microstructure and mechanical properties is high-speed nanoindentation mapping. Current nanoindentation systems enable the mechanical characterization of microstructures via rapid mapping of hardness and elastic modulus with sub-micron resolution across a millimeter-scale area.

This advance has sparked numerous studies on mechanical microstructure characterization on a wide range of topics from combinatorial investigations on diffusion couples [29] to the extra-terrestrial microstructures of meteors [30]. Nanoindentation mapping has also been applied to study the microstructure and individual phase properties in duplex steels with varying processing conditions [31,32]. Other nanoindentation studies on steel have characterized the precipitation of bainite [33], the χ-phase [34], and the ferrite–pearlite microstructure [35] emerging from thermomechanical processing. Nanoindentation mapping was also employed to study materials fabricated by AM. The local mechanical properties of a Ti-alloy fabricated by directed energy deposition [36] and Al-alloys fabricated by cold-spray AM [37] have been characterized.

In this work, the microstructures and mechanical properties of FFFm 316L steel 3D prints are investigated as a function of processing parameters using state-of-the-art nanoindentation mapping and analytical electron microscopy. The influence of the binder polymer content and heating rate during thermal debinding, sintering temperature, and atmosphere on the microstructure is investigated. Finally, the tensile properties of the 3D-printed 316L are characterized and compared with literature data from both additive and conventional fabrication routes.

2. Experimental procedure

2.1. Material preparation

Filaments were prepared by mixing gas-atomized AISI 316L powder (Sandvik Osprey Ltd., UK, D50 = 2.8 μm, nominal composition see Supplementary Information Table S1) with a multi-component binder into feedstocks. The feedstock consists of 316L powder, stearic acid surfactant (SA, Sigma-Aldrich, USA), a soluble thermoplastic elastomer (TPE, Kraiburg AG, German), a partially soluble polyethylene with a melt flow rate of 70 g/10 min (PE70, Arkema, France), and a insoluble polyethylene with a melt flow rate of 2.63 g/10 min (PE3, Arkema, France). The detailed procedure of the binder development was published in a previous work [38]. The exact feedstock compositions of all specimens can be found in the Supplementary Information in Table S2.

Tensile specimens were printed on a commercial fused filament fabrication 3D printer (Hephestos 2, BQ, Spain) using the commercial Simplify3D software. The geometry of the tensile specimens can be found in the Supplementary Information (Fig. S1). A nozzle with a diameter of 0.25 mm and a layer height of was 0.16 mm selected. The specimens were printed with a solid rectilinear infill, such that the infill is oriented with the long axis of the specimen. The print orientation was selected such that parts were lying flat on the print bed. The nozzle temperature was set to 230 °C and a temperature of 60 °C was used for the print bed. The print speed was chosen to be 280 mm min^{-1} and the extrusion multiplier was 1.

Partial removal of the binder was performed by solvent debinding in cyclo-hexane at 60 °C for 7 h using a magnetic stirrer at 120 rpm. After solvent debinding the specimens were dried in air for 24 h and the mass loss was monitored.

Thermal debinding and sintering were performed in either a tube furnace (HTRH 40-100/16, Carbolite Gero GmbH & Co. KG, Germany) or a retort furnace (VHT 08/16-Mo, Nabertherm GmbH, Germany). Details on the retort furnace used can be found in [39]. The influence of the sintering conditions were studied using cylindrical feedstock specimens (D = 1.8 mm, L = 5 mm) and the following temperature profile: Heating from room temperature to 370 °C at 5 K/min; heating to 490 °C at a rate of 0.5 K/min or 5 K/min; 10 h dwell; heating to the sintering temperature (1200 °C, 1250 °C, 1300 °C, 1350 °C) at 5 K/min; 3 h dwell; furnace cooling (average rate 8 K/min between 1000 °C and 700 °C), in forming gas (5 % H_2–Ar of 99.95 % purity, or H_2 of 99.999 % purity at 12 L h^{-1}).

In the retort furnace the following temperature profile was used: Heating from room temperature to 340 °C at 2 K/min; heating to 490 °C at 0.5 K/min; 3 h dwell, heating to 1360 °C at 5 K/min; 3 h dwell; cooling at an average rate of 60 K/min between 1000 °C and 700 °C, in H_2 atmosphere 99.999 % purity at 100 L h^{-1}. The thermal cycles employed in these heat treatments are illustrated schematically in Supplementary Figure S2. All sintering experiments were performed on Al_2O_3 substrates.

The influence of the polymer binder fraction on the resulting microstructure was investigated, by using green bodies with an effective backbone content of 10 vol.% and 23 vol.%, which were subjected to solvent debinding, and one containing 50 vol.%, which was not subjected to solvent debinding.

The term effective backbone content refers to the binder fraction remaining in the compound after solvent debinding. This is slightly larger than the nominal backbone content of insoluble polymer due to interactions between different constituents [38]. Note that the 50 vol.% specimens had the same feedstock composition as the 23 vol.% specimens. Throughout this study the term *binder content* will be used to refer to the amount of binder before thermal debinding. Initially, all feedstocks contain 50 vol.% of binder and 50 vol.% of solid loading. The sintering conditions for each specimen are listed in Table 1.

2.2. Materials characterization

Cross-sections of the sintered steel specimens were prepared by embedding in Bakelite (LaborPress-3, Struers GmbH, Switzerland), followed by grinding and polishing (RotoPol-21, Struers GmbH, Switzerland, SiC 300, 600, 1200, 2400, 4000; diamond suspension 3 μm, 1 μm, 0.25 μm; Al_2O_3 suspension 50 nm). Specimens used for EBSD analysis were additionally polished by broad ion beam milling (IM4000, Hitachi Ltd., Japan).

The thermal decomposition of the binder was studies by thermogravimetric analysis (TGA) (Jupiter F3 STA 449, Netzsch GmbH & Co. KG, Germany). Feedstock specimens were heated to 700 °C at 5 K/min in an Ar atmosphere in both as-extruded condition and after solvent debinding. The temperature cycle for thermal debinding was designed based on the results of the TGA experiments.

High-speed nanoindentation mapping was performed using a KLA iNano system (KLA Instruments, USA) with a diamond Berkovich indenter. Square grids of 10,000 indents were created with an applied maximum load of 5 mN and an inter-indent spacing of 2 μm. The target load was selected based on continuous stiffness method indentation experiments to ensure that the maximum indentation depth was approximately 200 nm, resulting in a ratio of 1:10 between the depth and the spacing of the indents. This ratio has been found to provide the

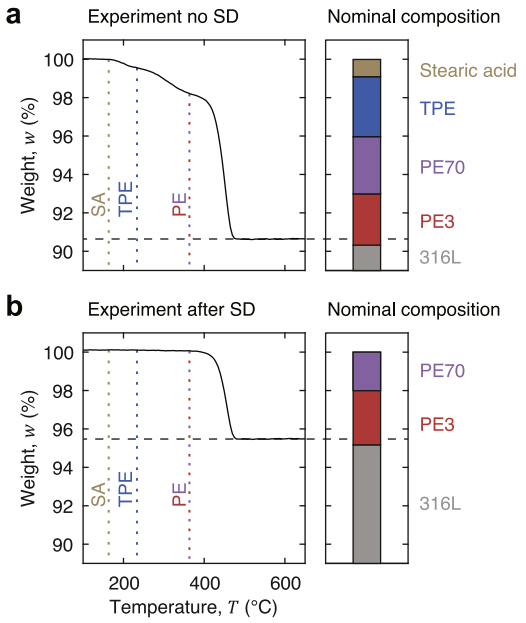

Fig. 1. TGA of the feedstock before **(a)** and after **(b)** solvent debinding (SD). The vertical dotted lines mark the onset of the thermal decomposition of the respective binder constituent. The experimentally measured weight loss coincides well with the nominal compositions (right). During solvent debinding, the SA and TPE components are removed completely and the PE70 is removed partially.

optimum resolution, while preventing significant interaction between the plastic zones of adjacent indents [40].

Microstructural analysis was performed using a combination of optical and electron microscopy. Polished cross-sections were first characterized by optical microscopy (AX10 Imager.M2 m, Zeiss, Germany). Sample porosity was measured optically on micrographs using ImageJ and by Archimedes immersion method in water (ASTM B962). In addition, the porosity was determined from the hardness and modulus contrast of the nanoindentation experiments (details can be found in the Supplementary Information Fig. S3).

Sintered microstructures were also investigated using scanning electron microscopy (SEM) (JSM-7100F, JEOL Ltd., Japan) and energy dispersive X-ray analysis (EDX) (Ametek-EDAX detector). Note that the presented EDX maps, were post processed to improve the visibility of the spatial variation in chemical composition.

Electron backscatter diffraction (EBSD) characterization was performed with an FEI Quanta F200 SEM equipped with an EDAX Hikari detector. Grains smaller than 500 nm were filtered out in the inverse pole figure maps during post processing.

Large scale mechanical testing was performed using tensile tests, on specimens sintered according to Table 1 I, on a universal testing machine (Schenck RSA 100, Schenck, Germany) equipped with a 100 kN load cell at a strain rate of $0.1\ \mathrm{min}^{-1}$. Five specimens were tested. The strain was measured optically.

The carbon content of the primary powder and of sintered specimens with varying polymer contents was measured by hot gas extraction (LECO CS230, LECO Corporation, USA). Four specimens of the powder were tested and two specimens for each sintering condition.

3. Results

3.1. Effect of thermal debinding conditions

The thermal decomposition of the binder is studied before and after solvent debinding by TGA. By comparing the experimentally measured weight loss to the nominal compositions, it can be determined if the two-step debinding process can effectively remove the polymeric binder. The TGA experiment of pure stearic acid can be found in the Supplementary Information Fig. S4, showing a complete thermal decomposition between 160 °C and 260 °C. The thermal decomposition of the TPE takes place between 300 °C and 460 °C(see Supplementary Information of [38]).

Table 1
Parameters used in the different sintering routes. A-H were performed in the tube furnace, I was performed in the retort furnace.

ID	Binder content vol.%	$\dot{T}_{pyro}$ K min^{-1}	T_s °C	Atmosphere	$\dot{T}_{\downarrow}$ K min^{-1}
A	23	0.5	1350	H_2–Ar	8.8
B	23	5	1350	H_2–Ar	8.8
C	10	5	1350	H_2–Ar	8.8
D	50	5	1350	H_2–Ar	8.8
E	23	5	1200	H_2–Ar	8.8
F	23	5	1250	H_2–Ar	8.8
G	23	5	1300	H_2–Ar	8.8
H	23	0.5	1350	H_2	8.8
I	23	0.5	1360	H_2	88

The observed weight loss is slightly lower than expected for both conditions (Fig. 1). This is ascribed to the evaporation of stearic acid during mixing of the feedstock at 180 °C. The weight loss from the thermal decomposition of stearic acid (Fig. 1a) is also smaller than the expected 0.9 wt.% of the nominal feedstock composition. Hence, the total organic weight fraction after compounding and extrusion is slightly lower. After solvent debinding, no shoulders indicating the pyrolysis of stearic acid and TPE are found (Fig. 1b). The PE70 component is only partially removed by solvent extraction, which was also found in a previous study on the development of the binder system [38]. The carbon content in the sintered steel is not affected by the amount of binder removed by pyrolysis (Table 2). The primary powder contains 130 wt.ppm of carbon. In the sintered steel, the carbon content amounts to 10–30 wt.ppm, indicating significant decarbonization.

The influence of the binder content and the heating rate during thermal decomposition on the microstructure was also investigated. Fig. 2a–d shows optical micrographs of the polished cross sections, prepared from the sintering conditions shown in Table 1A–D.

The binder content is found to have a large effect on the formation of defects. A binder fraction of 10 vol.% results in cracks with a length of several hundred micrometers (Fig. 2c). Specimens with a high polymer content of 50 vol.% show large spherical voids. In specimens with a binder content of 23 vol.%, no large defects are observed.

No clear trends in behavior were observed with the heating rate during pyrolysis (Fig. 2a, b). Specimens fabricated with a heating rate of 5 K/min and a binder content of 23 vol.% and 50 vol.% showed open blisters on the surface after sintering. The blistering phenomenon can be avoided by using a binder content of 23 vol.% in combination with a heating rate of 0.5 K/min or a binder content of 10 vol.%. Supplementary Figure S5 shows SEM micrographs of severe blister formation on the surface for high binder content and the absence of blisters on a specimen's surface containing 10 vol.% of binder, both heated at 5 K/min.

To investigate local variations in mechanical properties, high-speed nanoindentation was used (Fig. 2e, g). Based on the hardness and modulus variations, the data is segmented into clusters representing individual component phases. These phases are identified using the mechanical data in combination with EDX, EBSD, and the respective sintering conditions. Further, the phases can be distinguished by hardness and modulus in a 2D histogram (Fig. 2g, phases are indicated by labels).

Across all sintered specimens, the austenitic matrix, exhibits an average hardness of 2.6–3.6 GPa and average modulus of 170–200 GPa. The coefficient of variation of the average hardness of the austenite phase (excluding porosity and secondary phases) between different

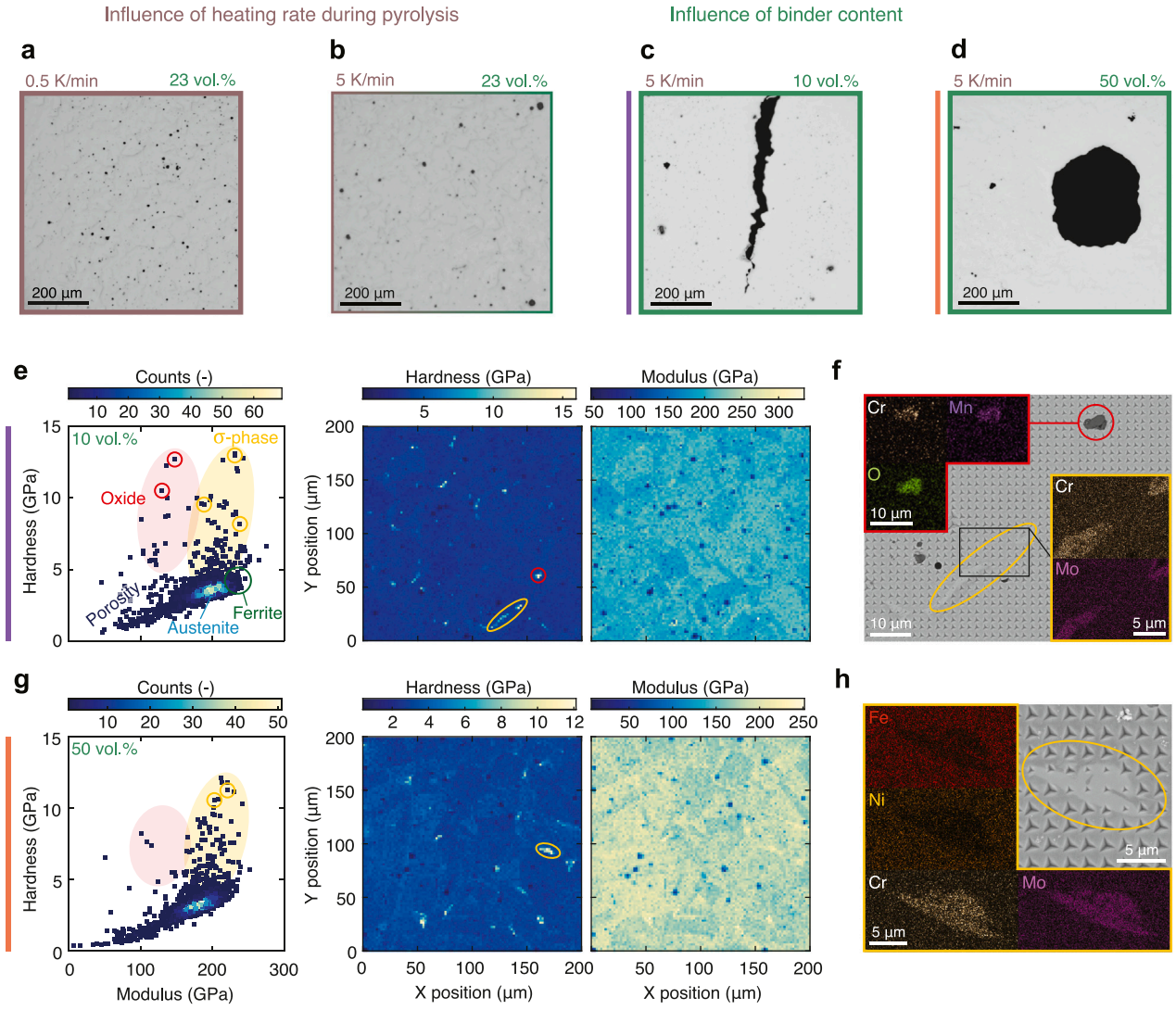

Fig. 2. (a–d) Polished cross-sections of 316L specimens with both varying binder contents and debinding at different heating rates. **(e, g)** Hardness and modulus data from high-speed nanoindentation mapping of a specimen with 10 vol.% and 50 vol.% of binder. In the 2D histogram different phases are labeled. **(f, h)** SEM back scatter electron contrast and EDX investigation of the different phases identified by nanoindentation.

Table 2
Average carbon content of 316L measured by hot gas extraction. A significant loss in carbon is observed during sintering independent of the binder volume fraction.

	Primary powder	Sintered 10 vol.% binder	Sintered 23 vol.% binder	Sintered 50 vol.% binder
Carbon (wt.ppm)	130	10	30	20

sintering conditions amounts to 13 %. A brief discussion of the variation in hardness can be found in the Supplementary Information (Fig. S6).

The oxide phase (red) has a hardness of up to 15 GPa and a modulus of about 100–180 GPa. σ-phase precipitates (yellow) are located between the austenite grains with a hardness of up to 13 GPa and a modulus of about 180–240 GPa. The larger degree of scatter in the values of the oxide and the σ-phase is due to their small size, which results in indentation volumes that have a mixture of the secondary phase and the matrix. δ-ferrite (green) can be identified as an intergranular phase with a hardness of 3.5–4.5 GPa and a modulus of 180–240 GPa, which are both slightly higher than the austenite matrix.

Indentations which fall in or on the edges of porosity result in both decreased hardness and modulus. Hence, the porosity appears as scattering tail towards lower properties, since they are represented as mixture between solid metal and air. Single grains can be differentiated within both hardness and modulus maps, and even some twins can be perceived due to the plastic and elastic anisotropy of austenite. The oxide phase appears to be less prevalent in specimens which contained a 50 vol.% polymer (Fig. 2g) than in the 10 vol.% specimens (e).

The microstructural features identified in the indentation maps were further investigated by using analytical electron microscopy (Fig. 2f). In the micrographs, the oxide phase appears much darker than the austenite phase in both secondary electron and the back scattered electron contrast. The σ-phase is slightly brighter than the austenite in back scattered electron contrast (Fig. 2f, h). EDX analysis shows that the red phase is a Cr–Mn oxide. The σ-phase (yellow) is enriched in Cr and Mo, while being slightly depleted in Fe and Ni.

3.2. Effect of sintering temperature

The influence of the sintering temperature on the microstructure was investigated according to Table 1 B, E-G. An increase of the temperature from 1200 °C to 1300 °C showed no significant effect on the density and microstructure (Fig. 3a–c). Again an oxide phase (red) is detected by nanoindentation mapping (Fig. 3e, g) and SEM micrograph (f) independent of temperature. The results of the indentation experiments of 1200 °C and 1250 °C specimens can be found in the Supplementary Information (Fig. S7). Data points with greatly increased hardness and modulus are found for sintering below 1350 °C, marked blue in the 2D histogram. SEM investigation of the corresponding locations reveals that these data points are artifacts, which can be attributed to indentation of large open pores. For calculation of hardness and modulus, the initial contact point between the indenter and the surface is assumed to happen at the tip apex. This not the case for indentations in porosity, as it is shown in Fig. 3f. Consequently, the contact area used for calculation is too small, leading to an overestimation of hardness and modulus. No signs of Cr–Mo rich σ-phase or δ-ferrite are observed in specimens sintered at temperatures below 1350 °C.

Sintering at 1350 °C results in a significant increase in density (Fig. 3d). Pores are located inside of austenite grains. This is typical for the final sintering stage [8]. The density, measured optically, by analysis of indentation data, and by Archimedes immersion method, as a function of the sintering temperature is plotted in Fig. 3h. Specimens sintered below 1350 °C have an average density of 87 %. Sintering temperatures of 1350 °C and 1360 °C result in an average sintering density above 96 %. Archimedes immersion measurements of specimens sintered at 1360 °C in pure H_2 yield an average density of 97 %.

3.3. Effect of sintering atmosphere and cooling rate

Atmosphere and cooling rate can have a significant effect on the sintering behavior. Two types of reducing sintering atmospheres were explored under the conditions listed in Table 1 A, H and I. As reported in the previous sections, the specimen sintered in a forming gas (5 % H_2–Ar) atmosphere exhibit an oxide phase (red) dispersed in the austenite matrix (Fig. 4d, e). However, no signs of an oxide phase could be detected in specimens sintered in high purity H_2 atmosphere (Fig. 4f, g).

While specimens cooled with a rate of 8 K/min, exhibit a hard σ-phase enriched in Cr and Mo (yellow), there is no such phase in specimens cooled at 60 K/min (see Fig. 4g). Instead of the σ-phase, intergranular δ-ferrite with both increased hardness and modulus is present. The δ-ferrite is enriched in Cr and Mo and depleted in Ni. Specimens cooled at a lower rate exhibit the σ-phase and the ferritic phase directly adjacent to each other (Fig. 4e, bottom). The yellow dashed line indicates the boundary between the two phases. Below the line, the yellow phase is present, marked by higher hardness, increased brightness in back scattered electron contrast, and the chemical composition. Above the line, a darker ferritic phase only slightly harder than the austenite parent phase can be observed.

Twins are clearly visible in the modulus contrast of specimens cooled at a rate of 8 K/min (Fig. 4d, f), while the specimen cooled at a rate of 60 K/min does not show any signs of twins. This is surprising as the formation of annealing twins takes place during grain growth [41], so it should not be affected by the cooling rate. It has been reported that an increase in carbon content can reduce twinning in 316 and 316L stainless steels [42]. The specimen without twins (Fig. 4g) was sintered in the retort furnace, while the other specimens were sintered in the tube furnace. Hence, a difference in carbon level is possible. Plastic deformation can also induce twinning. Although the grinding and polishing process was kept as consistent as possible, an influence cannot be fully excluded.

Fig. 5 depicts EBSD and EDX maps of the oxide phase (a–c) and a precipitate of δ-ferrite–σ-phase (d–g) in a specimen sintered using the conditions listed in Table 1 A. The orientation of the grains is shown in inverse pole figure orientation maps overlaid with the EBSD image quality map (b, d). Large angle grain boundaries are marked black. A cubic crystal structure was detected for the particulate oxides (highlighted red), which was not further indexed. The surrounding matrix is FCC austenite. BCC ferrite precipitations are found at junctions of austenite grains. The Cr–Mo-rich σ-phase did not yield diffraction patterns. The phases found in the sintered steel can be illustrated by overlaying the SEM micrograph with the hardness map (Fig. 5h). Each indent, corresponding to a distinct phase (austenite, ferrite, σ-phase, oxide and pores), can be connected to its location in a cluster of the 2D histogram.

Table 3
Comparison of mechanical properties of 316L stainless steel fabricated by different manufacturing rout. Ultimate tensile strength (UTS) and Elongation at break (A) are mean values if a standard deviation is provided. The data of this work contains five tensile tests of 3D-printed tensile specimens sintered with conditions shown in Table 1.

Ref.	UTS MPa	UTS std. MPa	A %	A std. %	Fabrication technique
This work	561	10	64	2	FFFm
Gong, 2018	465		31		FFFm
Liu, 2020	441	27	29.5	3.8	FFFm
Damon, 2019	522	7	38	1	FFFm
Safka, 2020	561		53		FFFm
Caminero, 2020	498.6	3.4	37.1	1.2	FFFm
Wang, 2021	540		59		FFFm
Wang, 2018	483		14		Pellet extrusion
Frykholm, 2016	511		58		Binder jet
Frykholm, 2016	520		50		MIM
Wang, 2018	520		24		MIM
Berginc, 2006	508		62		MIM
Gong, 2018	648		30		SLM
Bryant, 2017	600		28		SLM
Safka, 2020	620		43		SLM
Schumacher, 2021	685		37		SLM
Yadollahi, 2015	640		36		DED

3.4. Mechanical properties of 316L steel fabricated by FFFm

The tensile properties of 3D-printed and sintered 316L steel (sintering conditions Table 1 I) were measured. Stress–strain curves are found to be very consistent between the five specimens tested (Fig. 6a). The material shows good ductility, with an average elongation at failure of 64 ± 2 %. The average ultimate tensile strength amounts to 561 ± 10 MPa. The specimens showed extensive necking prior to fracture. The fracture surface (Fig. 6c) shows a dimpled pattern at two length scales: micron-scale and sub-micron scale. The material shows excellent properties, both in terms of elongation at failure and tensile strength, in comparison to literature values (Fig. 6b) for other sintered 316L fabricated by fused filament fabrication of metals (FFFm) [4,11,12,43–45], metal injection molding (MIM) [46–48], pellet extrusion (PE) [46], binder jetting (BJ) [47], and values reported for the bulk material (S) [49,50]. 316L fabricated by selective laser melting (SLM) [43,44,51,52] or directed energy deposition (DED) [53] exhibits higher tensile strengths at the expense of lower ductility, due to rapid quenching of the melt. Table 3 shows the numerical valued of the mechanical properties corresponding to Fig. 6b.

4. Discussion

4.1. Thermal debinding and sintering of 316L steel

Thermal debinding:

Precise control of the binder content and heating rate is required to achieve defect-free thermal debinding. Partial removal of the binder during solvent debinding lowers the amount of organic material to be removed by subsequent thermal decomposition. At the same time,

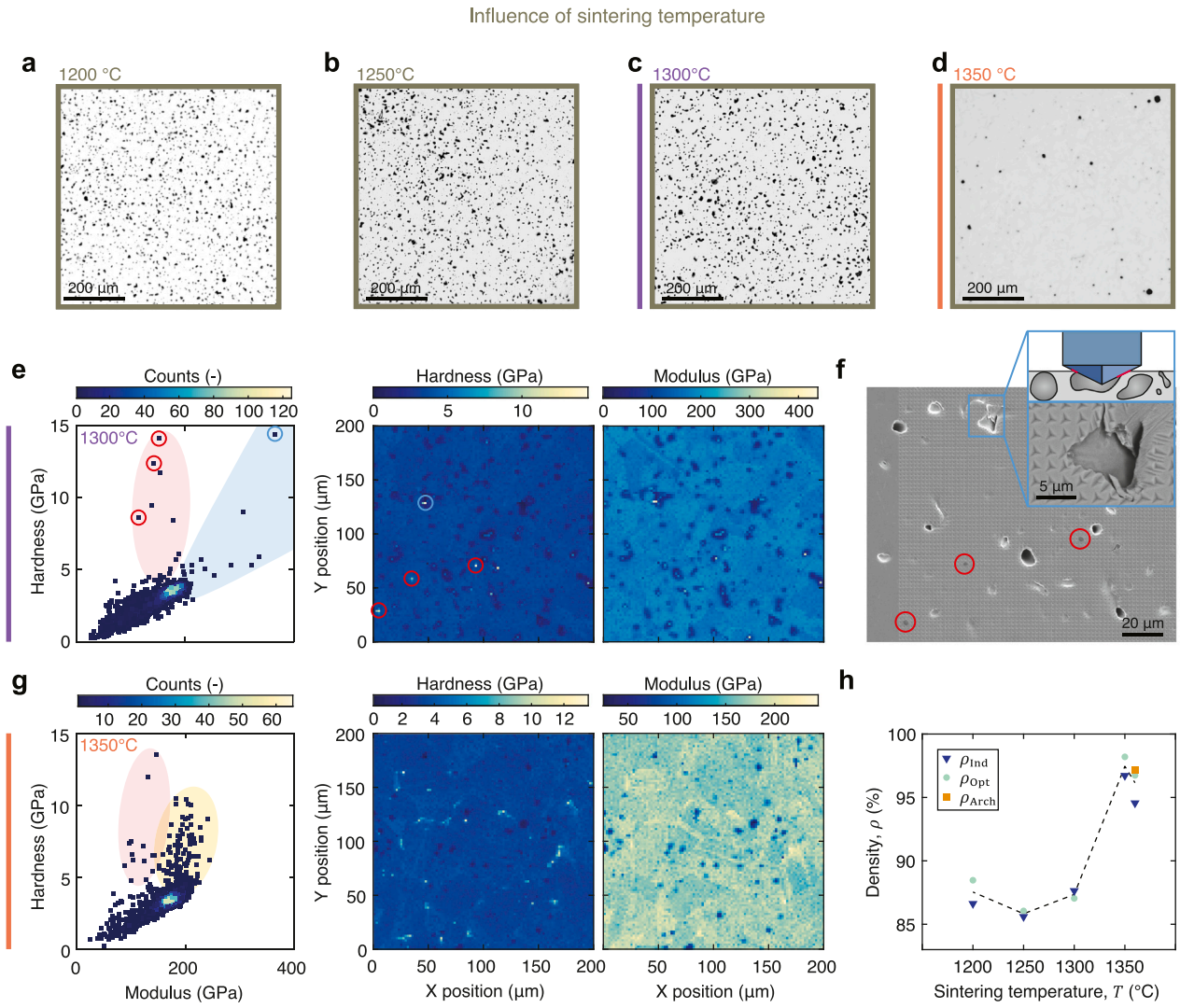

Fig. 3. (a–d) Cross-sectional analysis of 316L specimens sintered at different temperatures. **(e, g)** Hardness and modulus data from high-speed nanoindentation mapping of a specimen sintered at 1300 °C and 1350 °C. The oxide phase (red) is present independent of the sintering temperature. Data points highlighted blue, are artifacts from indentation of large open pores. The hard Cr–Mo-rich phase (yellow) is exclusively present in specimens sintered at 1350 °C. **(f)** SEM investigation of the indented area of the specimen sintered at 1300 °C. **(h)** Sintering densities obtained by thresholding of light microscopy images, processing of nanoindentation data, and Archimedes measurements. Sintering at temperatures of 1350 °C and above result in a significantly higher density. (For interpretation of the references to color in this figure legend, the reader is referred to the web version of this article.)

solvent debinding introduces a percolating network of open pores, which facilitates the outgassing of decomposition products from the bulk. TGA investigations show that the soluble TPE and SA can be effectively removed by solvent debinding, while the partially soluble PE70 and the insoluble PE3 remain as the effective backbone (Fig. 1).

The amount of backbone is decisive for the prevention of defects during debinding. A low effective backbone content of 10 vol.% causes crack formation (Fig. 2c), most likely due to stresses from swelling of the polymers during solvent debinding. This is in good agreement with earlier findings [38]. The backbone needs to provide sufficient green strength in order to prevent these types of defects [54].

Specimens with 50 vol.% binder, which were not subjected to solvent debinding, exhibit large spherical defects several hundred micrometers in size (Fig. 2d). As the 50 vol.% specimens were not subjected to solvent debinding, no network of open pores is present during thermal debinding. Thus, blister defects are formed by the entrapment gaseous products of the pyrolysis [55]. Blistering is also greatly affected by the heating rate during thermal debinding. Surface blisters are found for a high heating rate of 5 K/min during pyrolysis of samples with binder contents of 23 vol.% and 50 vol.%. This demonstrates that defect-free debinding requires a careful tuning of both the backbone content and the heating rate during pyrolysis to allow exit of gaseous products prior to sintering.

Reduction of oxides during sintering:

Nanoindentation and SEM examinations both show a hard particulate phase (red) in all specimens which were sintered in a 5 % H_2–Ar atmosphere, regardless of sintering temperature. EDX analysis reveals that this phase contains O, Cr, and Mn. On the surface of the powder particles, a continuous shell of stable oxides protects the alloy from oxidation. Some studies have reported nanometer-sized particulate oxides, containing Cr, Mn, and other highly reactive alloying elements on the surface of powder particles [56]. During sintering these stable oxides can grow at expense of less stable iron oxide due to internal getter effects [57]. The oxide particles can then move along grain boundaries and coalesce into larger agglomerates. Particulate oxides are known to have a detrimental embrittlement effect on mechanical properties [58].

The primary powder initially exhibits a smooth surface without any indication of oxide agglomerates (Supplementary Information Fig. S7). After sintering, the particulate oxides have a size of ~ 5 µm. EBSD analysis of the oxide phase (Fig. 5a-c) shows a cubic crystal structure.

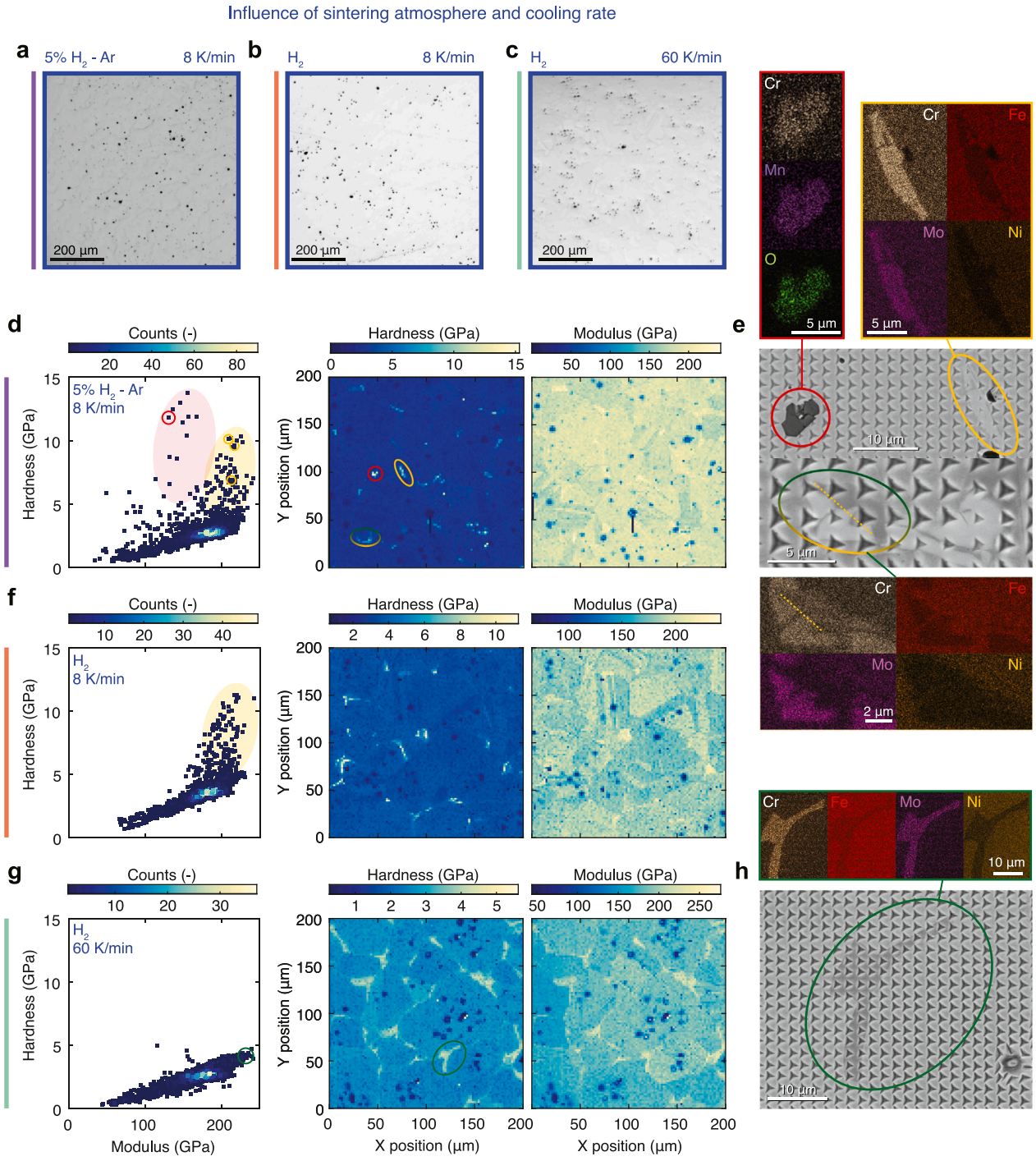

Fig. 4. **(a–c)** Light microscopy images of 316L sintered in 5 % H_2–Ar forming gas and pure H_2, and cooled at different rates. **(d, f, g)** Nanoindentation mapping data corresponding to the three micrographs. The oxide phase (red) is only found in the forming gas specimen. The hard Cr–Mo-rich phase (yellow) is not present in the specimen cooled at 60 K/min. Instead, an extensive intergranular ferritic phase (green) is dispersed in the austenite matrix. The ferrite phase is present at a lower extent in the specimen cooled at 8 K/min. **(e, h)** SEM and EDX analysis of the phases identified by indentation. (For interpretation of the references to color in this figure legend, the reader is referred to the web version of this article.)

Considering this in combination with EDX characterization results, it appears likely that the detected oxide is a spinel, commonly observed in Cr-alloyed steels. Cubic spinels include Cr_3O_4, $MnCr_2O_4$ and $FeCr_2O_4$, which can also show an enrichment of Si [59,60]. Oxides containing elements with high oxygen-affinity also exhibit high thermodynamic stability. Thus, their reduction during sintering is difficult. As these oxide phases are still observed in specimens sintered in 5 % H_2–Ar atmosphere, this indicates that the gas oxidization degree, i.e. the ratio of H_2O to H_2, of the atmosphere was too high for complete reduction of the oxide phase.

Another factor in the reduction under these conditions is the residual carbon from the pyrolysis of the binder. The carbon-monoxide forming reaction exhibits a high Gibbs free energy of formation at the sintering temperature (see Ellingham diagram [61]), which can act to reduce the oxide phase. Nanoindentation results from the specimen with 10 vol.% (Fig. 2e) shows more oxide phase than the 50 vol.% binder specimen (g). Higher binder contents during thermal debinding result

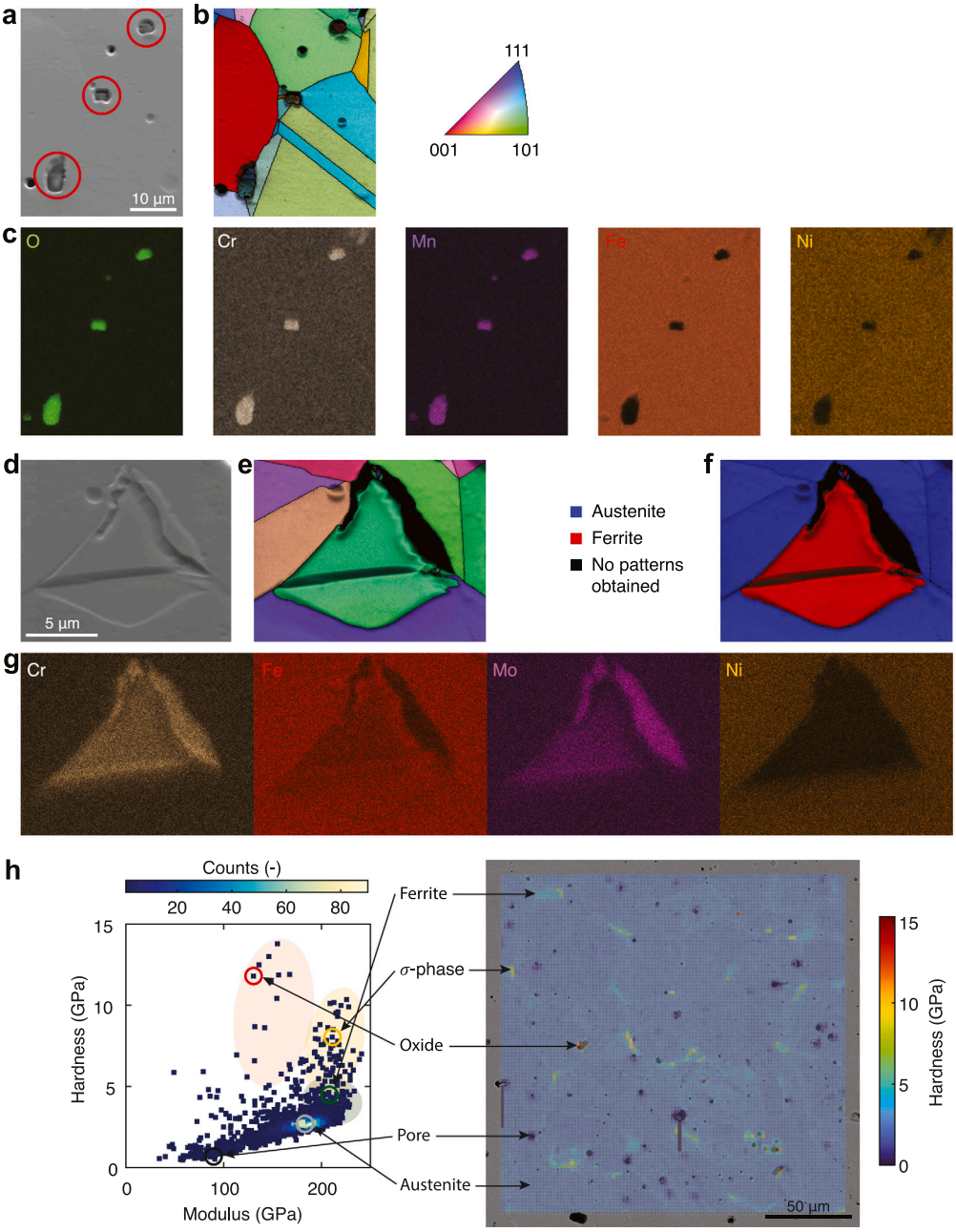

Fig. 5. **(a–c)** EBSD and EDX mapping of the oxide phase found in a 316L specimen prepared according to Table 1 A. The inverse pole figure is overlaid with the image quality. A cubic crystal structure is found for the oxide phase surrounded by FCC austenite. **(d–g)** EDX and correlated EBSD mapping of ferrite and σ precipitation found in the same specimen. The σ-phase (region of highest Cr and Mo content) did not yield diffraction patterns. **(h)** SEM micrograph of the indentation map of the same specimen, overlaid with the hardness mapping (right). Different phases are identified and assigned to data clusters in the 2D histogram (left).

in more residual carbon and consequently more reduction. This should be confirmed by measuring the oxide content of sintered steel with different fractions of binder.

The carbon reduction hypothesis is supported by the quantification of carbon in the primary powder and in the sintered steel (Table 2). The carbon content decreases significantly during sintering and shows no correlation with the binder content during thermal debinding. This suggests that the residual carbon reacts with the Cr–Mn oxides and potentially with the oxygen in the sintering atmosphere [62–64]. The carbon content after sintering is then determined by the amount of oxygen or water vapor in the sintering atmosphere, which can vary slightly between different experimental runs.

To obtain complete reduction of all oxide phases, a switch to a H_2 (99.999 % purity) sintering atmosphere was required. The gas oxidation degree of the pure H_2 furnace atmosphere is sufficiently low to allow reduction of stable spinel oxides. This is demonstrated by the absence of oxide phases in the nanoindentation maps in Fig. 4f, h. *Effect of sintering temperature on density and microstructure:*

The major feature of the sintering density plot in Fig. 3h is the pronounced increase in density from 87 % to 96 % observed on increasing the sintering temperature from 1300 °C to 1350 °C. This phenomenon in steel sintering has been attributed to the precipitation of intergranular ferrite in the austenitic matrix, which enhance the sintering kinetics [65]. This occurs for two reasons, first, the lattice-diffusion is faster in ferrite than in austenite. Second, the newly introduced δ - γ phase boundaries provide additional pathways for accelerated diffusion. This same mechanism is harnessed to accelerate densification during sintering of Ti, where the temperature can be cycled across the

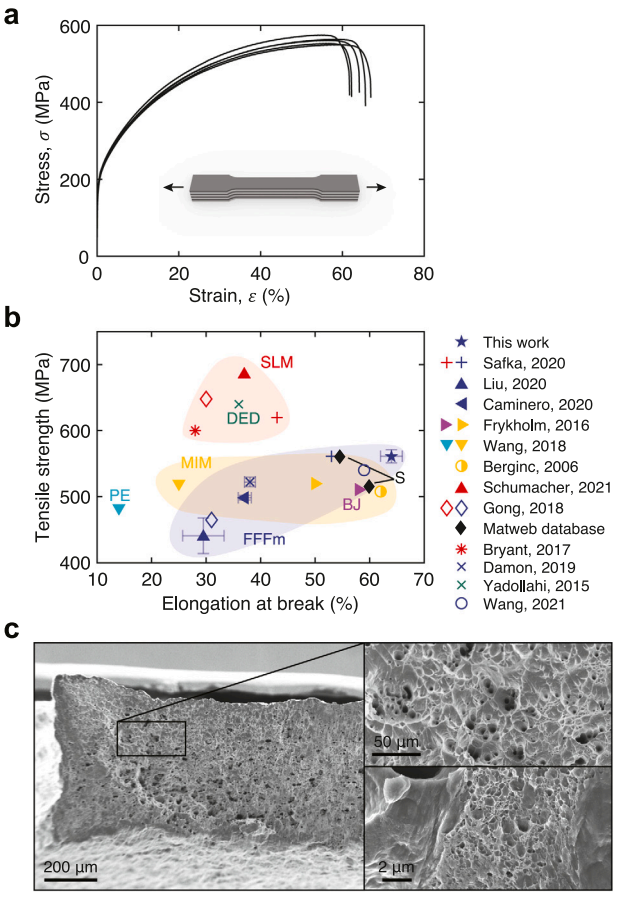

Fig. 6. **(a)** Tensile tests of 3D-printed 316L specimens fabricated according to Table 1 J. **(b)** Comparison of the experimentally measured ultimate tensile strength and elongation at failure with literature data (selective laser melting (SLM), directed energy deposition (DED), pellet extrusion (PE), fused filament fabrication of metals (FFFm), binder jet printing (BJ) and standard values of bulk 316L (S)). **(c)** The fracture surface exhibits a pronounced hierarchical dimple pattern, indicating a ductile failure mechanism.

α - β transition [66]. EBSD analysis (Fig. 5f) confirms the presence of the intergranular ferritic phase. Further, EDX mapping shows that the ferritic phase is enriched in ferrite-stabilizing Cr and Mo, and depleted in austenite-stabilizing Ni (Fig. 6g). According to the ternary Cr-Ni-Fe phase diagram [67],at 70 wt.% Fe, no equilibrium δ-ferrite should be expected in 316L alloys at room temperature. However, local variations in composition due to the segregation of Cr or Mo and small amount of ferrite nuclei from rapid solidification during gas atomization may induce the formation of a ferritic phase [68]. The compositions segregation of these ferrite-stabilizing elements during sintering is likely the reason why δ-phase is retained after cooling to room temperature.

σ-phase formation:

A third hard phase is also observed in specimens sintered at temperatures of 1350 °C and cooled at 8 K/min, independent of the sintering atmosphere. More rapidly cooled specimens (cooling rate of 60 K/min) do not exhibit this hard phase (Fig. 4g). EDX spectroscopy shows the phase to be enriched in Cr and Mo but with a reduced Ni and Fe concentration relative to the austenitic matrix. No diffraction patterns could be obtained using EBSD (Fig. 5e, f) possibly due to nanocrystalline grains smaller than the volume sampled by EBSD.

Based on the conditions of the formation and the observed chemical composition, this hard phase is most likely a σ-phase intermetallic. The σ-phase is present over a wide range of compositions in the Fe–Cr–Mo ternary diagram [69]. It forms during dwelling or slow cooling at temperatures from 700 °C to 1000 °C [70]. The formation kinetics in homogenized austenitic stainless steel are very slow, as the process is nucleation controlled [71], and δ - γ phase boundaries act as nucleation sites for the transformation of ferrite into σ and γ [70,71]. This is consistent with the σ-phase being exclusively observed in slow cooled specimens sintered at 1350 °C. Specimens sintered at lower temperatures lack the ferrite phase providing nucleation sites. EDX maps in Fig. 5g show a depleted zone of Mo and Cr at the interface between ferrite and σ-phase with a slight Fe enrichment. This suggests that Cr and Mo diffuse from the ferrite into the σ-phase, while Fe diffuses in the opposite direction. In some regions, the ferrite phase is completely transformed into σ and γ (Fig. 2f, h, Fig. 4e (top)), but in others, both the ferritic and the σ-phase still coexist next to each other (Fig. 4e (bottom), Fig. 5d–g).

Despite exhibiting a considerable fraction of δ-ferrite, no signs of σ-phase are seen in the specimens sintered at 1360 °C and cooled with 60 K/min. This is ascribed to the faster cooling rate, suppressing the precipitation of the σ-phase. In 22005 duplex steel, the precipitation of the σ-phase is reported for cooling rates below 12 K/min, while cooling rates above 60 K/min largely suppress a precipitation [72]. This is consistent with our observations and suggests duplex and 316L steels have similar precipitation kinetics, if a δ-phase is present in the latter. Precipitation of the hard σ-phase in stainless steels is highly undesirable, as it causes embrittlement [73–75], and reduces the corrosion resistance by depleting the local Cr and Mo content around σ precipitates [76,77]. Therefore, high cooling rates are suggested in order to prevent σ precipitation.

4.2. Mechanical properties of 316L steel fabricated by FFFm

To assess the relative mechanical performance of the FFFm 316L steel, both the measured ultimate tensile strength and elongation at failure are compared with literature values of 316L steel fabricated by various techniques (Fig. 6b). By both mechanical metrics, FFFm steel of this work is comparable to the values for bulk 316L (marked with S), even surpassing the elongation at failure. The mechanical properties observed in here differ significantly from the ones reported for the more widespread beam-based techniques, which typically exhibit lower ductility and higher ultimate strength. The difference can be explained by the non-equilibrium microstructures obtained from beam-based techniques, exhibiting fine microstructures of solidification cells and columnar grains, which together with precipitates is known to have strengthening effects, while lowering the ductility [78]. Sintering-based approaches like FFFm on the contrary, have microstructures closer to equilibrium with more equiaxed grains [6]. Hence, the strength is lower, mechanical properties are more isotropic, and larger strains at failure can be achieved.

The excellent ductility displayed by our FFFm steel is a direct result of the absence of embrittling hard phases, which is corroborated by the dimpled morphology of the fracture surface (Fig. 6c) showing extensive micro-void coalescence. Often, precipitates of secondary phases, like particulate oxides, are found inside of dimples, as they act as nucleation sites for micro-voids [58], but this could not be observed this case. This shows the success of the optimized processing conditions during 3D printing and sintering (Table 1 I). However, the good mechanical properties of the sintered 316L may come at the cost of corrosion resistance, since some intergranular δ-ferrite phase is present in the optimized steel. This ferrite depletes the surrounding austenite of Cr and Mo and likely reduces its corrosion resistance.

Many materials fabricated by FFFm suffer from large inter-layer pores. However, no such pores are found on the fracture surface of our FFFm material. Large pores between adjacent layers and strands of deposited material are a major source for anisotropy in metals fabricated by FFFm [4,12]. If this process-induced porosity can be prevented, by optimization of the deposition parameters, the material properties are isotropic.

4.3. Nanoindentation as a characterization tool

Nanoindentation mapping proved to be a useful characterization tool for the detection of secondary phases during the sintering optimization study of FFFm 316L steel. This is highlighted in Fig. 5h, which depicts a 2D histogram showing the identified phases correlated with an electron micrograph of the indentation grid with the hardness map overlaid. EDX correlation allows easy segmentation of the hardness and modulus data into distinct phases: austenite, δ-ferrite, σ-phase, and spinel oxides. Additionally, individual grains and twins can be observed in the matrix phase, and porosity can be easily characterized.

As porosity is a concern in many AM processes, including FFFm, we developed a first approach to extract quantitative values for porosity from the hardness and modulus contrast by means of statistical analysis. This method allows quantification of the surface fraction of any phase, but here it is used to quantify porosity by assuming porosity behaves as a phase with hardness and modulus values of zero. Good agreement is observed with the established optical analysis and Archimedes immersion method (Fig. 3h).

The quantification of porosity based on nanoindentation data is associated with certain limitations. First, subsurface pores can be detected if they are sufficiently close to the surface to affect the stress field. Second, the pore size could be overestimated by false classification of indents from the vicinity of a pore. And third, the minimum detectable pore size is limited by the resolution, i.e. the size of the stress field determining the minimum spacing between indents. It should be noted that the phases measures here all have a characteristic size detectable using a 2 µm spacing between indents. While the first and second points can be remedied by adjusting the empirical threshold values of hardness and modulus in the data analysis, the latter is a fundamental restriction inherent to nanoindentation. Theoretically, the statistical analysis can be also applied to the other phases identified. Phase deconvolution may be difficult if phases show a considerable overlap in modulus and hardness.

5. Conclusions

This study investigates the microstructures and mechanical properties evolving from the sintering of 316L filaments for 3D printing. It was demonstrated that through careful optimization of the sintering parameters detrimental phases (oxides and σ-phase) can be avoided and high sintering densities can be obtained. The sintered material exhibits excellent mechanical properties compared to literature data for both conventional and AM materials.

In contrast to beam-based AM steels, the FFFm 316L steel demonstrated here has a more equilibrium microstructure without residual stresses. In combination with the low mechanical anisotropy demonstrated previously [38], it can be concluded that properly optimized FFFm processes allow the fabrication parts with microstructures and mechanical properties more analogous to conventional, bulk 316L steel.

Our findings suggest that the binder fraction is an important consideration, which can produce significant microstructural effects, e.g. by partial reduction of stable spinel oxides through residual carbon. This implies that the sacrificial role of the binder could be expanded and rethought in many techniques: powder injection molding and additive manufacturing processes like FFFm, ink writing, or binder jetting. Functional binders containing metal–organic frameworks or ceramic precursors could introduce additives in the sintering process to enable tuning of the resulting microstructures. Potential applications could include reduction agents, sintering aids, alloying elements, or a finely dispersed phase for grain boundary pinning.

Nanoindentation in combination with EDX mapping is shown to be a useful tool for microstructural investigations of the phase evolution of 316L in the sintering process. Detrimental phases such as pores, δ-ferrite, spinel oxides, and σ precipitates were easily identified in the indentation data from various sintering conditions. Further examination using scanning electron microscopy did not detect any additional phases in the material, which were not found by nanoindentation. An algorithm for phase quantification based the hardness and modulus contrast was developed and applied to measure the porosity with results in good agreement with conventional methods.

CRediT authorship contribution statement

Marius A. Wagner: Writing – review & editing, Writing – original draft, Visualization, Methodology, Investigation, Formal analysis, Data curation, Conceptualization. **Jona Engel:** Writing – review & editing, Investigation, Formal analysis. **Amir Hadian:** Writing – review & editing, Investigation, Formal analysis. **Frank Clemens:** Writing – review & editing, Formal analysis. **Mikel Rodriguez-Arbaizar:** Writing – review & editing, Investigation. **Efrain Carreño-Morelli:** Writing – review & editing. **Jeffrey M. Wheeler:** Writing – review & editing, Writing – original draft, Investigation, Formal analysis. **Ralph Spolenak:** Writing – review & editing, Supervision, Funding acquisition.

Declaration of competing interest

The authors declare that they have no known competing financial interests or personal relationships that could have appeared to influence the work reported in this paper.

Data availability

Data will be made available on request.

Acknowledgments

The authors would like to acknowledge the numerous contributions to this work. Dr. Fabio Krogh and Beatrice Wegmann contributed by building experimental set-ups and by scientific discussion. Gregor Mikel has performed the hot gas extraction measurements of the carbon content. Micha Calvo, Joan Sendra and Oliver Bruni have supported this study with experimental work and scientific discussion. The authors also acknowledge support of the Scientific Center for Optical and Electron Microscopy (ScopeM) of the ETH Zurich. Dr. Karsten Kunze needs to be mentioned especially, who has performed EBSD examinations. This study is part of the strategic focus area advanced manufacturing project “Sustainable Design of 4D Printed Active Systems (SD4D)” of the ETH domain, Switzerland.

Appendix A. Supplementary data

Supplementary material related to this article can be found online at https://doi.org/10.1016/j.addma.2022.103147.

References

[1] P. Nidheesh, M.S. Kumar, An overview of environmental sustainability in cement and steel production, J. Cleaner Prod. 231 (2019) 856–871.
[2] P. Wang, et al., Efficiency stagnation in global steel production urges joint supply-and demand-side mitigation efforts, Nature Commun. 12 (1) (2021) 1–11.
[3] M. Grasso, B.M. Colosimo, Process defects and in situ monitoring methods in metal powder bed fusion: A review, Meas. Sci. Technol. 28 (4) (2017) 044005.
[4] J. Damon, S. Dietrich, S. Gorantla, U. Popp, B. Okolo, V. Schulze, Process porosity and mechanical performance of fused filament fabricated 316L stainless steel, Rapid Prototyp. J. (2019).
[5] B. Zheng, et al., On the evolution of microstructure and defect control in 316L SS components fabricated via directed energy deposition, Mater. Sci. Eng. A 764 (2019) 138243.
[6] N. Tuncer, A. Bose, Solid-state metal additive manufacturing: A review, Jom (2020) 1–22.
[7] A. Bose, et al., Traditional and additive manufacturing of a new tungsten heavy alloy alternative, Int. J. Refractory Metals Hard Mater. 73 (2018) 22–28.
[8] R.M. German, Sintering Theory and Practice, 1996.

[9] A. Bautista, F. Velasco, M. Campos, M. Rabanal, J. Torralba, Oxidation behavior at 900°C of austenitic, ferritic, and duplex stainless steels manufactured by powder metallurgy, Oxidation Metals 59 (3) (2003) 373–393.

[10] K. Weman, Welding Processes Handbook, Elsevier, 2011, pp. 191–206.

[11] B. Liu, Y. Wang, Z. Lin, T. Zhang, Creating metal parts by fused deposition modeling and sintering, Mater. Lett. 263 (2020) 127252.

[12] Y. Wang, L. Zhang, X. Li, Z. Yan, On hot isostatic pressing sintering of fused filament fabricated 316L stainless steel–evaluation of microstructure, porosity, and tensile properties, Mater. Lett. 296 (2021) 129854.

[13] A. Watson, J. Belding, B.D. Ellis, Characterization of 17-4 PH processed via bound metal deposition (BMD), in: TMS 2020 149th Annual Meeting & Exhibition Supplemental Proceedings, Springer, 2020, pp. 205–216.

[14] M.Á. Caminero, A.R. Gutiérrez, J.M. Chacón, E. García-Plaza, P.J. Núñez, Effects of fused filament fabrication parameters on the manufacturing of 316l stainless-steel components: Geometric and mechanical properties, Rapid Prototyp. J. (ahead-of-print) (2022).

[15] M. Quarto, M. Carminati, G. D'Urso, Density and shrinkage evaluation of AISI 316L parts printed via FDM process, Mater. Manuf. Process. 36 (13) (2021) 1535–1543.

[16] A. Boschetto, L. Bottini, F. Miani, F. Veniali, Roughness investigation of steel 316L parts fabricated by metal fused filament fabrication, J. Manuf. Process. 81 (2022) 261–280.

[17] C. Burkhardt, P. Freigassner, O. Weber, P. Imgrund, S. Hampel, Fused filament fabrication (FFF) of 316L green parts for the MIM process, World PM2016-AM-Depos. Technol. (2016).

[18] D. Jiang, F. Ning, Additive manufacturing of 316L stainless steel by a printing-debinding-sintering method: Effects of microstructure on fatigue property, J. Manuf. Sci. Eng. 143 (9) (2021).

[19] M. Sadaf, M. Bragaglia, F. Nanni, A simple route for additive manufacturing of 316L stainless steel via fused filament fabrication, J. Manuf. Process. 67 (2021) 141–150.

[20] Y. Thompson, J. Gonzalez-Gutierrez, C. Kukla, P. Felfer, Fused filament fabrication, debinding and sintering as a low cost additive manufacturing method of 316L stainless steel, Addit. Manuf. 30 (2019) 100861.

[21] A. Vishwanath, K. Rane, J. Schaper, M. Strano, R. Casati, Rapid production of AZ91 Mg alloy by extrusion based additive manufacturing process, Powder Metall. 64 (5) (2021) 370–377.

[22] M. Coffigniez, et al., Modeling of interstitials diffusion during debinding/sintering of 3D printed metallic filaments: Application to titanium alloy and its embrittlement, Acta Mater. 219 (2021) 117224.

[23] Y. Thompson, et al., Fused filament fabrication-based additive manufacturing of commercially pure titanium, Adv. Energy Mater. 23 (12) (2021) 2100380.

[24] M.Q. Shaikh, S. Graziosi, S.V. Atre, Supportless printing of lattice structures by metal fused filament fabrication (MF3) of Ti-6Al-4V: Design and analysis, Rapid Prototyp. J. (2021).

[25] P. Singh, V.K. Balla, A. Gokce, S.V. Atre, K.H. Kate, Additive manufacturing of Ti-6Al-4V alloy by metal fused filament fabrication (MF3): Producing parts comparable to that of metal injection molding, Progr. Additive Manuf. 6 (4) (2021) 593–606.

[26] P. Singh, V.K. Balla, S.V. Atre, R.M. German, K.H. Kate, Factors affecting properties of Ti-6Al-4V alloy additive manufactured by metal fused filament fabrication, Powder Technol. 386 (2021) 9–19.

[27] J. Gonzalez-Gutierrez, et al., Bending properties of lightweight copper specimens with different infill patterns produced by material extrusion additive manufacturing, solvent debinding and sintering, Appl. Sci. 11 (16) (2021) 7262.

[28] E. Redondo, M. Pumera, Fully metallic copper 3D-printed electrodes via sintering for electrocatalytic biosensing, Appl. Mater. Today 25 (2021) 101253.

[29] J.M. Wheeler, B. Gan, R. Spolenak, Combinatorial investigation of the Ni–Ta system via correlated high-speed nanoindentation and EDX mapping, Small Methods (2021) 2101084.

[30] J.M. Wheeler, Mechanical phase mapping of the taza meteorite using correlated high-speed nanoindentation and EDX, J. Mater. Res. 36 (1) (2021) 94–104.

[31] H. Besharatloo, et al., Novel mechanical characterization of austenite and ferrite phases within duplex stainless steel, Metals 10 (10) (2020) 1352.

[32] H. Besharatloo, J.M. Wheeler, Influence of indentation size and spacing on statistical phase analysis via high-speed nanoindentation mapping of metal alloys, J. Mater. Res. 36 (11) (2021) 2198–2212.

[33] M. Yang, et al., Bainite percentage determination and effect of bainite percentage on mechanical properties in austempered AISI 5160 steel, Mater. Perform. Charact. 10 (1) (2021) 110–125.

[34] K. Wieczerzak, et al., An in situ and ex situ study of χ phase formation in a hypoeutectic Fe-based hardfacing alloy, Mater. Des. 188 (2020) 108438.

[35] S. Janakiram, P.S. Phani, G. Ummethala, S.K. Malladi, J. Gautam, L.A. Kestens, New insights on recovery and early recrystallization of ferrite-pearlite banded cold rolled high strength steels by high speed nanoindentation mapping, Scr. Mater. 194 (2021) 113676.

[36] Z. Liu, J. Zhang, B. He, Y. Zou, High-speed nanoindentation mapping of a near-alpha titanium alloy made by additive manufacturing, J. Mater. Res. 36 (11) (2021) 2223–2234.

[37] B.C. Sousa, M.A. Gleason, B. Haddad, V.K. Champagne, A.T. Nardi, D.L. Cote, Nanomechanical characterization for cold spray: From feedstock to consolidated material properties, Metals 10 (9) (2020) 1195.

[38] M.A. Wagner, et al., Fused filament fabrication of stainless steel structures-from binder development to sintered properties, Addit. Manuf. (2021) 102472.

[39] E. Carreño-Morelli, et al., Titanium parts by powder injection moulding of TiH2-based feedstocks, PIM Int. 4 (2010) 60–63.

[40] P.S. Phani, W. Oliver, A critical assessment of the effect of indentation spacing on the measurement of hardness and modulus using instrumented indentation testing, Mater. Des. 164 (2019) 107563.

[41] R.E. Smallman, A. Ngan, Physical Metallurgy and Advanced Materials, Elsevier, 2011, pp. 358–360.

[42] R. Varin, J. Kruszynska, Control of annealing twins in type 316 austenitic stainless steel, Acta Metall. 35 (7) (1987) 1767–1774.

[43] H. Gong, D. Snelling, K. Kardel, A. Carrano, Comparison of stainless steel 31L parts made by FDM-and SLM-based additive manufacturing processes, Jom 71 (3) (2019) 880–885.

[44] J. SAFKA, M. Ackermann, J. Machacek, M. Seidl, F. Véle, V. Truxová, Fabrication process and basic material properties of the basf ultrafuse 316lx material, MM Sci. J. 2020 (2020) 4216–4222.

[45] M.Á. Caminero, A. Romero, J.M. Chacón, P.J. Núñez, E. García-Plaza, G.P. Rodríguez, Additive manufacturing of 316L stainless-steel structures using fused filament fabrication technology: Mechanical and geometric properties, Rapid Prototyp. J. (2021).

[46] C. Wang, et al., Preparation of optimum degreasing–sintering process for metal–polymer blending low temperature 3D printing, Rapid Prototyp. J. (2019).

[47] R. Frykholm, Y. Takeda, B.-G. Andersson, R. Carlström, Solid state sintered 3-D printing component by using inkjet (binder) method, J. Japan Soc. Powder Powder Metall. 63 (7) (2016) 421–426.

[48] B. Berginc, Z. Kampus, B. Sustarsic, The influence of MIM and sintering-process parameters on the mechanical properties of 316l SS, Mater. Tehnol. 40 (5) (2006) 193.

[49] MatWeb material property data, 316L stainless steel, annealed bar, 2022, http://www.matweb.com/search/DataSheet.aspx?MatGUID=a2d0107bf958442e9f8db6dc9933fe31&ckck=1. (Accessed 30 January 2022).

[50] MatWeb material property data, 316L stainless steel, annealed plate, 2022, https://www.matweb.com/search/datasheet.aspx?MatGUID=530144e2752b47709a58ca8fe0849969. (Accessed 20 April 2022).

[51] Z. Brytan, Comparison of vacuum sintered and selective laser melted steel AISI 316L, Arch. Metall. Mater. 62 (2017).

[52] C. Schumacher, E. Moritzer, Stainless steel parts produced by fused deposition modeling and a sintering process compared to components manufactured in selective laser melting, in: Macromol. Symposia, 395, (1) Wiley Online Library, 2021, 2000275.

[53] A. Yadollahi, N. Shamsaei, S.M. Thompson, D.W. Seely, Effects of process time interval and heat treatment on the mechanical and microstructural properties of direct laser deposited 316L stainless steel, Mater. Sci. Eng. A 644 (2015) 171–183.

[54] S. Cano, et al., Additive manufacturing of zirconia parts by fused filament fabrication and solvent debinding: Selection of binder formulation, Addit. Manuf. 26 (2019) 117–128.

[55] K. Hwang, H. Lin, S. Lee, Thermal, solvent, and vacuum debinding mechanisms of PIM compacts, Mater. Manuf. Process 12 (4) (1997) 593–608.

[56] E. Hryha, C. Gierl, L. Nyborg, H. Danninger, E. Dudrova, Surface composition of the steel powders pre-alloyed with manganese, Appl. Surf. Sci. 256 (12) (2010) 3946–3961.

[57] C. Gierl-Mayer, R. de Oro Calderon, H. Danninger, The role of oxygen transfer in sintering of low alloy steel powder compacts: A review of the "internal getter" effect, Jom 68 (3) (2016) 920–927.

[58] D. Chasoglou, E. Hryha, L. Nyborg, Effect of process parameters on surface oxides on chromium-alloyed steel powder during sintering, Mater. Chem. Phys. 138 (1) (2013) 405–415.

[59] L. Kjellqvist, Thermodynamic description of the Fe-C-Cr-Mn-Ni-O system (Ph.D. thesis), KTH, 2009.

[60] I.-H. Jung, Critical evaluation and thermodynamic modeling of the Mn–Cr–O system for the oxidation of SOFC interconnect, Solid State Ion. 177 (7–8) (2006) 765–777.

[61] M. Hasegawa, Ellingham diagram, in: Treatise on Process Metallurgy, Elsevier, 2014, pp. 507–516.

[62] P. Wilyman, Sintering with nitrogen based atmospheres, Powder Metall. 28 (2) (1985) 85–89.

[63] S. Jauregi, F. Fernández, R. Palma, V. Martínez, J. Urcola, Influence of atmosphere on sintering of T15 and M2 steel powders, Metall. Trans. A 23 (2) (1992) 389–400.

[64] A. Hadian, C. Zamani, C. Schreiner, R. Figi, F.J. Clemens, Influence of carbon content and processing treatment of metallic binder on the outgassing and sintering of NbC based cemented carbide, Ceram. Int. 46 (18) (2020) 28422–28431.

[65] Y. Wu, D. Blaine, C. Schlaefer, B. Marx, R.M. German, Sintering densification and microstructural evolution of injection molding grade 17-4 PH stainless steel powder, Metall. Mater. Trans. A 33 (7) (2002) 2185–2194.

[66] R.M. German, Titanium sintering science: A review of atomic events during densification, Int. J. Refractory Metals Hard Mater. 89 (2020) 105214.
[67] K. Saeidi, X. Gao, F. Lofaj, L. Kvetková, Z.J. Shen, Transformation of austenite to duplex austenite-ferrite assembly in annealed stainless steel 316L consolidated by laser melting, J. Alloys Compd. 633 (2015) 463–469.
[68] T. Kurzynowski, K. Gruber, W. Stopyra, B. Kuźnicka, E. Chlebus, Correlation between process parameters, microstructure and properties of 316 l stainless steel processed by selective laser melting, Mater. Sci. Eng. A 718 (2018) 64–73.
[69] P. AF, R. PR, Decomposition of austenite in austenitic stainless steels, ISIJ Int. 42 (4) (2002) 325–327.
[70] Y. Maehara, Y. Ohmori, J. Murayama, N. Fujino, T. Kunitake, Effects of alloying elements on σ phase precipitation in δ–γ duplex phase stainless steels, Metal Sci. 17 (11) (1983) 541–548.
[71] J. Vitek, S. David, The sigma phase transformation in austenitic stainless steels, Weld. J. 65 (4) (1986) 106s–111s.
[72] H. Sieurin, R. Sandström, Sigma phase precipitation in duplex stainless steel 2205, Mater. Sci. Eng. A 444 (1–2) (2007) 271–276.
[73] M. El Koussy, I. El Mahallawi, W. Khalifa, M. Al Dawood, M. Bueckins, Effects of thermal aging on microstructure and mechanical properties of duplex stainless steel weldments, Mater. Sci. Technol. 20 (3) (2004) 375–381.
[74] Y. Ahn, J. Kang, Effect of aging treatments on microstructure and impact properties of tungsten substituted 2205 duplex stainless steel, Mater. Sci. Technol. 16 (4) (2000) 382–388.
[75] H. Sieurin, R. Sandström, Sigma phase precipitation in duplex stainless steel 2205, Mater. Sci. Eng. A 444 (1–2) (2007) 271–276.
[76] L. Karlsson, L. Ryen, S. Pak, Precipitation of intermetallic phases in 22% Cr duplex stainless weld metals, Welding J.-Incl. Weld. Res. Suppl. 74 (1) (1995) 28–38.
[77] K. Adhe, V. Kain, K. Madangopal, H. Gadiyar, Influence of sigma-phase formation on the localized corrosion behavior of a duplex stainless steel, J. Mater. Eng. Performance 5 (4) (1996) 500–506.
[78] P. Bajaj, A. Hariharan, A. Kini, P. Kürnsteiner, D. Raabe, E.A. Jägle, Steels in additive manufacturing: A review of their microstructure and properties, Mater. Sci. Eng. A 772 (2020) 138633.